Front. Energy 2022, 16(3): 471–482
https://doi.org/10.1007/s11708-021-0778-4

RESEARCH ARTICLE

**Haoxuan MA, Yuefa JIA, Jongseong BAE, Chunli LIU**

# Factors affecting photocatalytic performance through the evolution of the properties due to the phase transition from $NaBiO_3 \cdot 2H_2O$ to $BiO_{2-x}$



**Abstract** The phase transition process of a photocatalytic system from $NaBiO_3 \cdot 2H_2O$ to $BiO_{2-x}$ has been investigated to understand the important factors that affect photocatalytic performance in a composite system. It is found that a proper amount of $BiO_{2-x}$ on the surface of $NaBiO_3 \cdot 2H_2O$ could effectively suppress the electron/hole recombination and increase the exposed reactive sites for photocatalytic reaction. A fully covered $BiO_{2-x}$ on $NaBiO_3 \cdot 2H_2O$ results in a dramatical decrease of photocatalytic degradation of dye. An over long hydrothermal process can result in $BiO_{2-x}$ with reduced oxygen vacancies, which degrades the photocatalytic activity. Furthermore, the photocatalytic reduction ability of $CO_2$ conversion has been investigated, indicating that the surface activity to different reactants also directly affects the catalytic performance. The investigation of the gradient phase transition process presents a clear guidance to construct a desired photocatalytic system, in addition to selecting gradient materials with suitable bandgap structure and a morphology with different fraction and distribution of each component. The defect evolution of each component during construction of a composite is also an important factor that should be optimized and considered in making a composite to achieve high photocatalytic efficiency.

**Keywords** composite construction, distribution, $BiO_{2-x}$, evolution of defects

Received Apr. 26, 2021; accepted Jul. 19, 2021; online Sept. 25, 2021

Haoxuan MA, Yuefa JIA, Chunli LIU (✉)
Department of Physics and Oxide Research Center, Hankuk University of Foreign Studies, Yongin 17035, Republic of Korea
E-mail: chunliliu@hufs.ac.kr

Jongseong BAE
Busan Center, Korea Basic Science Institute, Busan 46742, Republic of Korea

## 1 Introduction

Due to the fast increase of the global energy consumption, solutions to relieve the server environmental pollution and energy has become an urgent need worldwide. Among various possible approaches, the water splitting, adsorption, and decomposition or conversion of pollutants into non-toxic or even useful fuels by using (photo)catalysts has been considered as promising directions [1–11].

In addition to $TiO_2$ or the single-phase photocatalytic system, many photocatalytic composite systems have been reported as potential strategies with efficient photocatalytic abilities, such as g-$C_3N_4$, bi-based nanomaterials, and various oxide semiconductors based composite system [12–19]. A majority of photocatalytic systems have been built by constructing two or more separated phased in a physical or hydrothermal process to investigate effective factors. However, most of the factors have been focused on the fraction and distribution of each component and the bandgap structures, but the property evolution of each component during coupling process has been ignored because usually no obvious change is presented in X-ray diffraction (XRD) or Fourier transform infrared spectrometer (FT-IR). Hence, to clearly understand the effective factors, constructing a heterojunction structure formed *in situ* should be the main choice, and *in situ* phase transition induced by calcination or doping have been used to construct such kind of composites [20–23]. Hydrothermal reaction has been explored to control the process of *in situ* phase transition. The phase transition from $NaBiO_3 \cdot 2H_2O$ to $BiO_{2-x}$ has been selected, due to the suitable band structures between $NaBiO_3 \cdot 2H_2O$ and $BiO_{2-x}$, and the gradient transition from $NaBiO_3 \cdot 2H_2O$ to $BiO_{2-x}$ could be regarded as an *in situ* (formation of a new gradient in the composite from the initial phase) growth of $BiO_{2-x}$ at the surface of $NaBiO_3 \cdot 2H_2O$. The remaining $[BiO_2]^-$ parts in $NaBiO_3$ could be easily transformed to $BiO_{2-x}$ after removal of $Na^+$ ions during a hydrothermal reaction

[24]. Furthermore, it is easy and convenient to investigate the evolution of $BiO_{2-x}$ during the transition process.

The bandgap energy of $BiO_{2-x}$ is about 1.6 eV [25], which extends the absorption range to visible and near-infrared light (NIR). In addition, since the oxygen defective $BiO_{2-x}$ possesses a 2D-like lattice structure, the oxygen vacancies can have more and stronger interactions with $O_2$ to form reactive oxygen species ($O_2^{-\bullet}$), and the oxygen defective content has been reported to have a determinant effect on the photocatalytic activity of $BiO_{2-x}$ [25,26]. Mostly, the $BiO_{2-x}$ phase is produced from the conversion of $NaBiO_3 \cdot 2H_2O$, and $NaBiO_3 \cdot 2H_2O$ itself is also a visible light photocatalyst with a bandgap of approximately 2.5 eV and suitable energy band positions [27]. The overpotentials of both $NaBiO_3 \cdot 2H_2O$ and $BiO_{2-x}$ than $O_2/(-0.13$ eV versus (normal hydrogen electrode) NHE) makes such composite more efficient to generate highly oxidizing superoxide ($O_2^{-\bullet}$), which can effectively decompose dye pollutants [28]. Various $BiO_{2-x}$ based heterojunctions, such as $Bi_2O_2CO_3$/graphene/$BiO_{2-x}$, $BiO_{2-x}$ /$Bi_2O_{2.75}$, $Bi_2O_4$-$Bi_4O_7$-$BiO_{2-x}$, core-shell-structured $Bi_2O_4$/$BiO_{2-x}$, $BiO_{2-x}$ /$NaBiO_3$ etc., have been proposed as highly efficient photocatalysts [29–33]. However, the conclusions only focus on the enhanced light absorption and charge separation efficiency with suitable band structures.

Through the study of gradient transition from $NaBiO_3 \cdot 2H_2O$ to $BiO_{2-x}$ by using a hydrothermal method with variation of the reaction time and the characterizations of the structural, optical, and photo-electrochemical properties, the results reported here could provide systematic information on the construction of photocatalytic composite systems. The factors affecting the photocatalytic performance have been determined by the orderly changes in the degradation efficiency of methyl orange. Finally, to investigate the photocatalytic reduction abilities, the measurements of photocatalytic $CO_2$ reduction in a solid/gas system have been conducted.

## 2 Experimental section

### 2.1 Materials

All of the chemicals for the synthesis of the catalysts were used without any further purification. Sodium bismuthate ($NaBiO_3 \cdot 2H_2O$, $w(NaBiO_3 \cdot 2H_2O) > 80\%$, $w$ is mass fraction), sodium hydroxide beads (NaOH, $w(NaOH) > 97\%$, $w$ is mass fraction) and methyl orange (MO) were purchased from the DAEJUNG company.

### 2.2 Synthesis of $NaBiO_3 \cdot 2H_2O$ (NBH)/$BiO_{2-x}$

The NBH/$BiO_{2-x}$ composite and $BiO_{2-x}$ were prepared by a hydrothermal method. 1 g of NBH was put into 30 mL of deionized (DI) water, then mixed with 20 mL of 1.6 mol/L NaOH solution for 1 h. The mixture was transferred to an 80 mL Teflon vessel sealed in a stainless autoclave and heated at 180°C for a certain time, and labeled as NB-$x$ ($x$ is the reaction time: 0, 1.5, 3, 5, 6, 7.5, 9, 12, 16, 21 h). After being cooled down in air to room temperature, the products were washed using DI water and ethanol, then dried in air at 60°C for 12 h. To investigate the effect of pH value (alkaline, neutral, and acidic conditions) during the synthesis process, deionized water or dilute nitric acid solvent (addition of 3 mL concentrated $HNO_3$) was also used instead of NaOH. The XRD and scanning electron microscopy (SEM) images of these samples were presented in Fig. S1 in Electronic Supplementary Material (ESM).

### 2.3 Characterizations

The crystal structures of the samples were characterized by a Rigaku MiniFlex 600 XRD using Ka ($\lambda$ = 0.15428 nm) radiation. FT-IR was recorded using a Nicolet Avatar 370 FT-IR to investigate the chemical bonds. The morphologies and elements distribution were characterized by SEM (Hitachi-S4800) and transmission electron microscopy (TEM) equipped with energy dispersive spectrometer (EDS) (JEOL, JEM-ARM200F). The X-ray photoelectron spectroscopy (XPS) characterizations were measured by using a monochromated Al Ka X-ray source ($hv$ = 1486.6 eV) at 15 kV/150 W to investigate the evolution of ion valence (Busan Center of Korea Basic Science Institute). The UV-vis diffuse reflectance spectra (UV-vis DRS) were performed on a U3010 UV-vis spectrometer to identify the visible light absorption ability and NIR absorption. The photoluminescence (PL) emission spectra were recorded with an excitation wavelength of 320 nm. The surface photovoltage (SPV) measurement was conducted on a surface photovoltage spectroscopy (CEL-SPS 1000, Beijing Perfect Light Technology Co., Ltd).

## 3 Results and discussion

The XRD patterns and FT-IR spectra are shown in Figs. 1(a) and 1(b). In Fig. 1(a), the spectrum labeled with a, b, c, d, e, f, g, h, i, and j presents the sample NB-0, NB-1.5, NB-3, NB-5, NB-6, NB-7.5, NB-9, NB-12, NB-16, and NB-21, respectively. The purchased NBH is used as NB-0. Obviously, NB-1.5–NB-9 exhibit two sets of XRD peaks from NBH and $BiO_{2-x}$, and the peak intensities of $BiO_{2-x}$ are enhanced with the reaction time, suggesting continuous conversion from $Bi^{5+}$ to $Bi^{3+}$. In NB-12, NB-16, and NB-21, all the diffraction peaks are matched well with the cubic phase of $BiO_{2-x}$ (JCPDS NO. 47-1057), indicating that all NBH has been converted to $BiO_{2-x}$ after 12 h of reaction.

The FT-IR characterization demonstrated a consistent phase transition with the XRD spectra. As displayed in

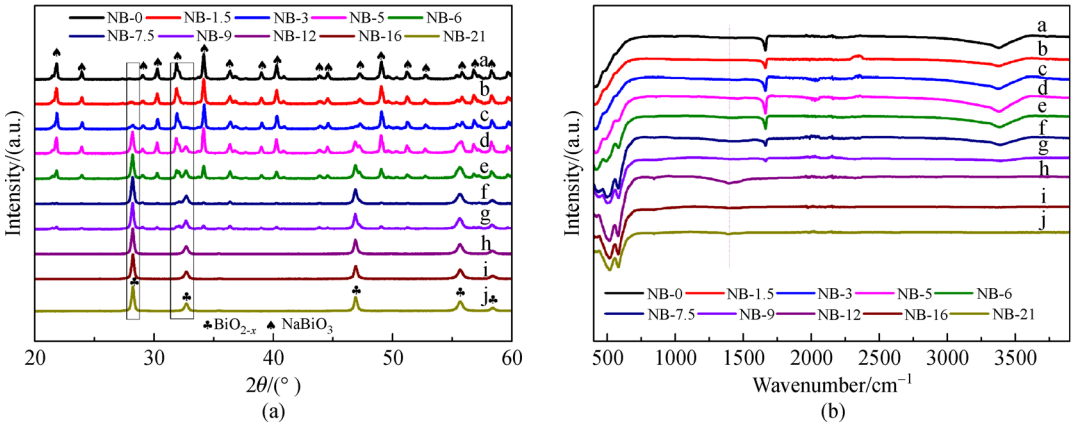


**Fig. 1** XRD patterns and FT-IR spectra of samples obtained at different times (a. NB-0 0 h, b. NB-1.5 1.5 h, c. NB-3 3 h, d. NB-5 5h, e. NB-6 6 h, f. NB-7.5 7.5 h, g. NB-9 9 h, h. NB-12 12 h, i. NB-16 16 h, j. NB-21 21 h).
(a) XRD patterns of samples; (b) FT-IR spectra of samples.

Fig. 2, NB-0 (curve a) exhibits characteristic peaks at 418, 482, and 566 $cm^{-1}$, which can be ascribed to the typical stretching vibration of bonds in $BiO_6$ octahedral units [34]. The broad peaks at 1620 and 3400 $cm^{-1}$ can be assigned to the stretching vibration mode of –OH. NB-12 (curve h) only reveals two strong peaks at 519 and 584$cm^{-1}$ [35], which can be attributed to the Bi–O bonds in $BiO_3$ pyramidal units. NB-1.5–NB-9 (curves b–g) exhibit two sets of FT-IR peaks as a combination of NBH and $BiO_{2-x}$, with a gradual increased intensity from $BiO_{2-x}$. Interestingly, a quite obvious peak located at 1493 $cm^{-1}$ only appears in NB-12, which can be attributed to the abnormal bond caused by the high density of oxygen vacancies in $BiO_{2-x}$ [36,37]. However, this peak becomes quite weak again in NB-16 and NB-21, implying that the oxygen vacancies could be filled up with a longer reaction time.

The phase transition from NBH to $BiO_{2-x}$ can also be clearly observed from the morphology change of the products. NB-0 shows worm like aggregated particles composed of irregular nanosheets (Fig. 2(a)), and $BiO_{2-x}$ shows a wall-like nanostructure made up of hexagonal nanoplates mostly perpendicular to each other (NB-12 to NB-21) [38]. The worm-like morphology is maintained till NB-6, indicating the dominant composition of NBH in the composite. It is expected that $BiO_{2-x}$ is formed from the NB-0 surface during the hydrothermal reaction. It can be seen in the high-resolution image of NB-1.5 (Fig. 2(b)) that there are some small and tiny plates of $BiO_{2-x}$ on the

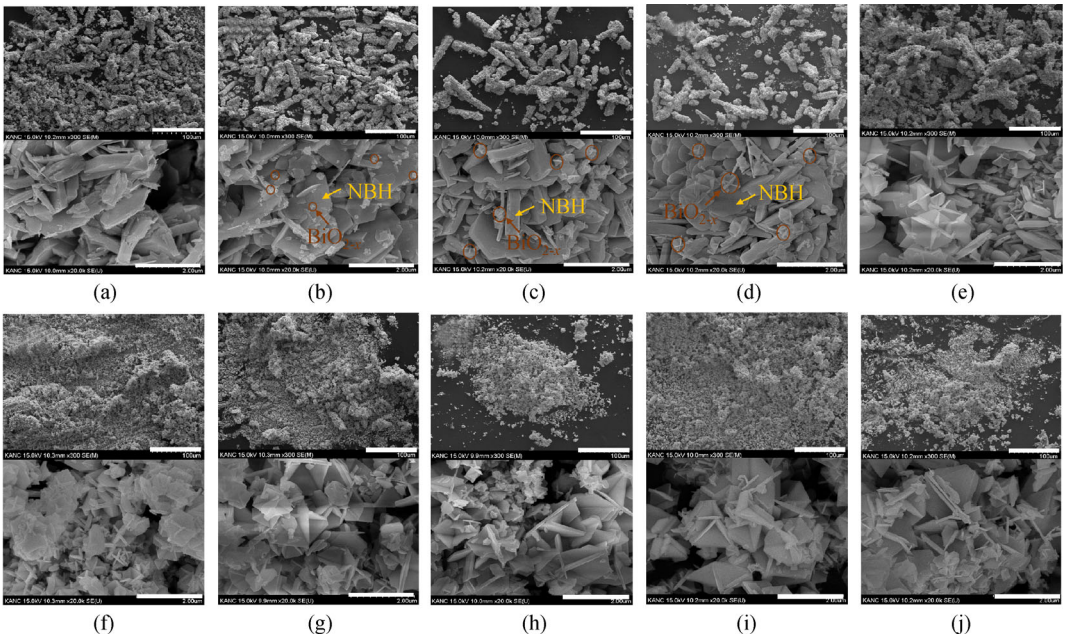


**Fig. 2** SEM images of reaction time dependent samples (longer scale bar: 2 μm; short scale bar: 100 μm).
(a) NB-0; (b) NB-1.5; (c) NB-3; (d) NB-5; (e) NB-6; (f) NO-7.5; (g) NB-9; (h) NB-12; (i) NB-16; (j) NB-21.

surface, and more and larger $BiO_{2-x}$ nanoplates in NB-3. In NB-6, abundant $BiO_{2-x}$ plates appear and cover most parts of the NBH surface. From NB-7.5 to NB-21, the worm-like structure disappears, indicating that $BiO_{2-x}$ becomes the dominant material in the composite.

The microstructures of NB-3, NB-6, and NB-12 measured by TEM are depicted in Fig. 3. In NB-3 (Fig. 3(a)), tiny and small hexagonal $BiO_{2-x}$ nanoplates are formed on the surface of irregular shaped NBH nanoparticles. In NB-6, it is not easy to observe NBH, which should be mostly covered by larger $BiO_{2-x}$ plates (Fig. 3 (b)). The TEM of NB-12 shows larger hexagonal $BiO_{2-x}$ nanoplates (nm) with sharp edges. The EDS-elemental mapping images and the corresponding elements ratio are collected in Fig. 4 and Table 1, respectively. A homogeneous distribution of Bi, O, and Na elements can be seen in all three samples. Table 1 shows that the percentage of Na element and the atomic ration (O/Bi) decreases with the reaction time till NB-12, implying the continued phase transition from NBH to $BiO_{2-x}$. The very low percentage of Na in NB-12, which could be attributed to the trace residual on the surface after washing, can be ignored. It is noted that the O/Bi atomic ratio in NB-16 is larger than the NB-12, most probably due to the filling of oxygen atoms into the oxygen vacancies caused by a longer reaction time, that is to say, NB-12 has more oxygen vacancies.

XPS characterization was performed on NB-0, NB-3, NB-6, and NB-12 to determine the specific bonding and the chemical states of the elements on the surface of the composition during the phase transition. The XPS wide scan spectra in Fig. 5(a) clearly demonstrate the existence of the Na, Bi, and O elements, and the percentage of each element is listed in Table 1 and the details in Table S1 (in ESM). The evolution tendency of the ratio between different elements are consistent with the EDS results listed in Table 1. Interestingly, the increasing atomic ratios of O/Bi from NB-6 to NB-21 indicate an increase of the oxygen concentration in $BiO_{2-x}$, i.e., some of the oxygen vacancies are filled, which may be mainly caused by the $O_2$ generated during the phase transition process (equations in ESM). In the EDS measurement, the relative atomic ratio of O/Bi in $BiO_{2-x}$ is smaller than that obtained from XPS. For the sample of NB-16, the two results from EDS and XPS are similar, therefore, it is speculated that the filling of oxygen vacancies is mainly a process from the surface of the sample to the inside. As shown in the high-resolution spectrum of C 1s in Fig. 5(b), only one clear peak appears at 284.6 eV in each sample due to the carbon impurities, and is taken as a standard reference for calibration [39]. High-resolution XPS curves of Bi 4f shown in Fig. 5(c) show an obvious peak evolution with the reaction time. Only two peaks at 158.45 and 163.80 eV can be observed in NB-0, which belong to the peaks of Bi 4f7/2 and Bi 4f5/2 of $Bi^{5+}$. In NB-3, NB-6, and NB-12, the peaks of Bi 4f can be de-convoluted well into four peaks at binding energies of 158.05, 163.35 eV, 158.45, and 163.80 eV, representing the $Bi^{3+}$ and $Bi^{5+}$ chemical states, respectively [40]. Obviously, the splitting of Bi 4f peaks with respect to the reaction time indicate an increased percentage of $Bi^{3+}$ chemical state due to the appearance of $BiO_{2-x}$. In the case of O 1s state shown in Fig. 5(d), the peaks can be de-convoluted into three peaks with binding energies of 529.24, 530.70, and 533.83 eV for the sample of NB-0, which are attributed to the lattice O in crystal, oxygen vacancy and absorbing water or crystal water [29]. Depending on the reaction time, the strongest peak at around 529.24 eV shifts to a lower binding energy due to the change in the O bonds environment induced by the phase transformation from NBH to $BiO_{2-x}$ (the transformation of $Bi^{5+}$-O to $Bi^{3+}$-O). In addition, the intensity of the peak at 533.83 eV decreased, due to the loss of crystal water during the hydrothermal reaction, which is consistent with the investigation of FT-IR. Obviously, the peak intensity at 530.7 eV increases from NB-0 to NB-12, indicating the continue formation of oxygen defective $BiO_{2-x}$. $BiO_{2-x}$ has an oxygen defective structure. Oxygen defects can cause changes in the structural environment of the surrounding lattice oxygen, mainly resulting in increased electron density of the surrounding oxygen, thereby the binding energy (529.10 eV) of part initial oxygen shift to a higher binding energy (530.70 eV). In general, this peak next to that of lattice oxygen is often used to indicate the strength of oxygen defects [41,42]. Furthermore, the high-resolution XPS spectra of O 1s and Bi 4f for the samples from NB-12 to NB-21 are shown in Fig. 6. No obvious difference can be observed, however,

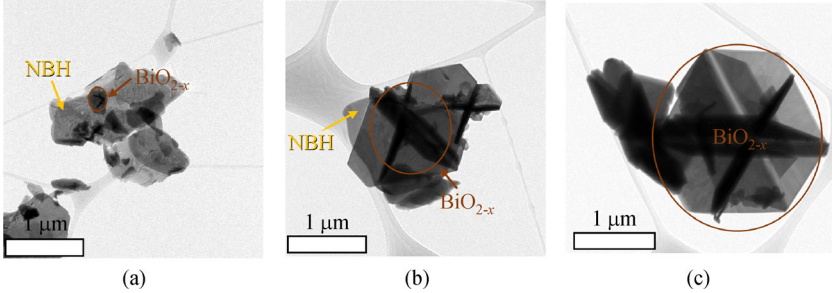


**Fig. 3** TEM images of reaction time dependent samples.
(a) NB-3; (b) NB-6; (c) NB-12.

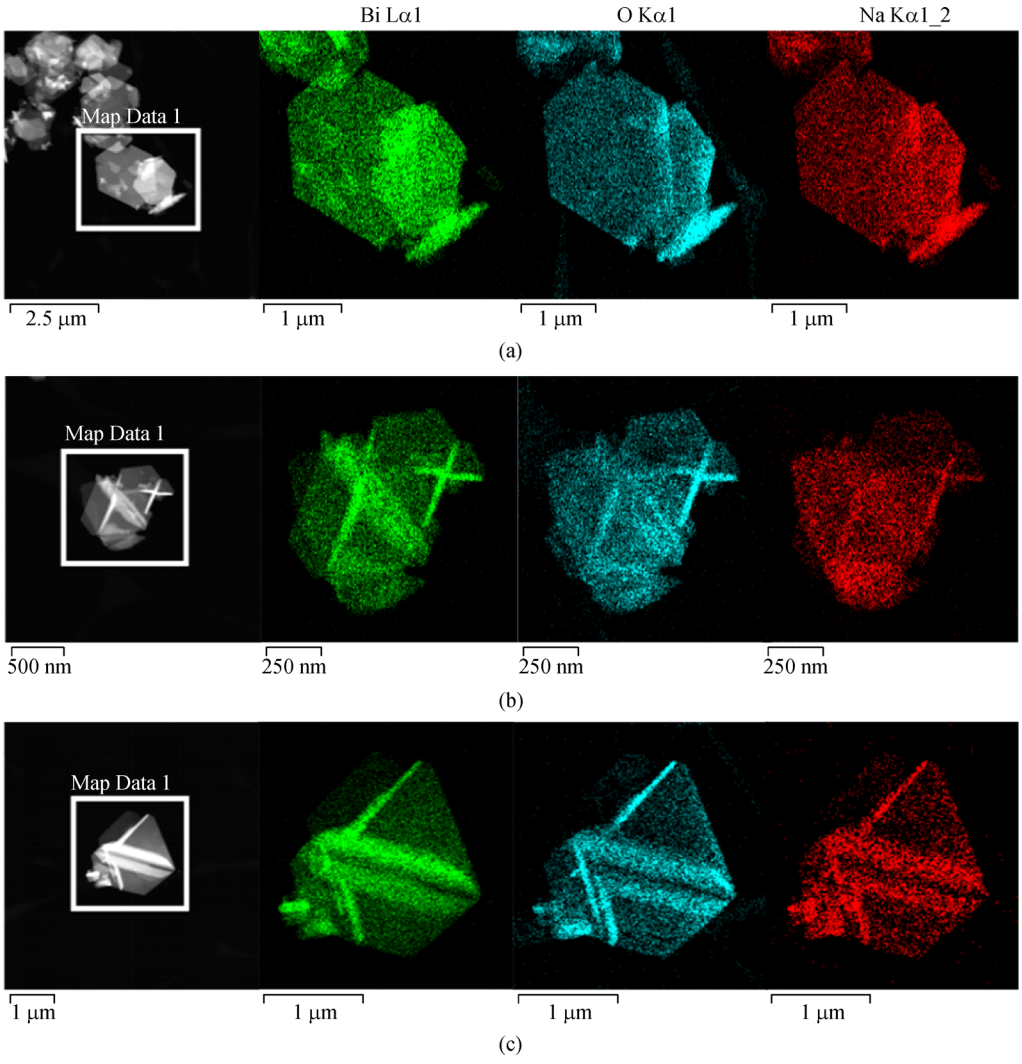


**Fig. 4** Elemental distribution maps for Bi, O, and Na of (a) NB-3, (b) NB-6, and (c) NB-12.

**Table 1** Elemental ratio measured by EDS and XPS for NB-3, NB-6, NB-12, and NB-16

| Element | NB-3/(Atomic fraction, %) | NB-6/(Atomic fraction, %) | NB-12/(Atomic fraction, %) | NB-16/(Atomic fraction, %) |
|---|---|---|---|---|
| O (EDS) | 56.73 | 61.41 | 50.28 | 55.06 |
| Na (EDS) | 17.15 | 8.64 | 2.99 | 3.05 |
| Bi (EDS) | 26.13 | 29.96 | 46.74 | 41.90 |
| Total: (EDS) | 100.00 | 100.00 | 100.00 | 100.00 |
| Atomic ratio: O/Bi (EDS) | 2.17 | 2.05 | 1.08 | 1.31 |
| Atomic ratio: O/Bi (XPS) | 1.49 | 1.32 | 1.31 | 1.34 |

the peaks of Bi 4f from NB-12 to NB-21 slightly shift to a lower binding energy, indicating that tiny of $Bi^{5+}$ changed to $Bi^{3+}$, as shown in Fig. 6(a). Besides, the intensity of the peak induced by oxygen vacancy decreases slightly, indicating that the content of defect is decreasing, as shown in Fig. 6(b). The investigations from XPS are consistent with the characterizations in the XRD and EDS measurements. The above characterizations reveal a clear view of structure and morphology change during the *in situ* phase transition from NBH to $BiO_{2-x}$, which is expected to affect the photocatalytic properties.

UV-vis DRS were taken from the samples to evaluate their optical properties, as presented in Fig. 7(a). The visible light absorption between 400 and 800 nm clearly

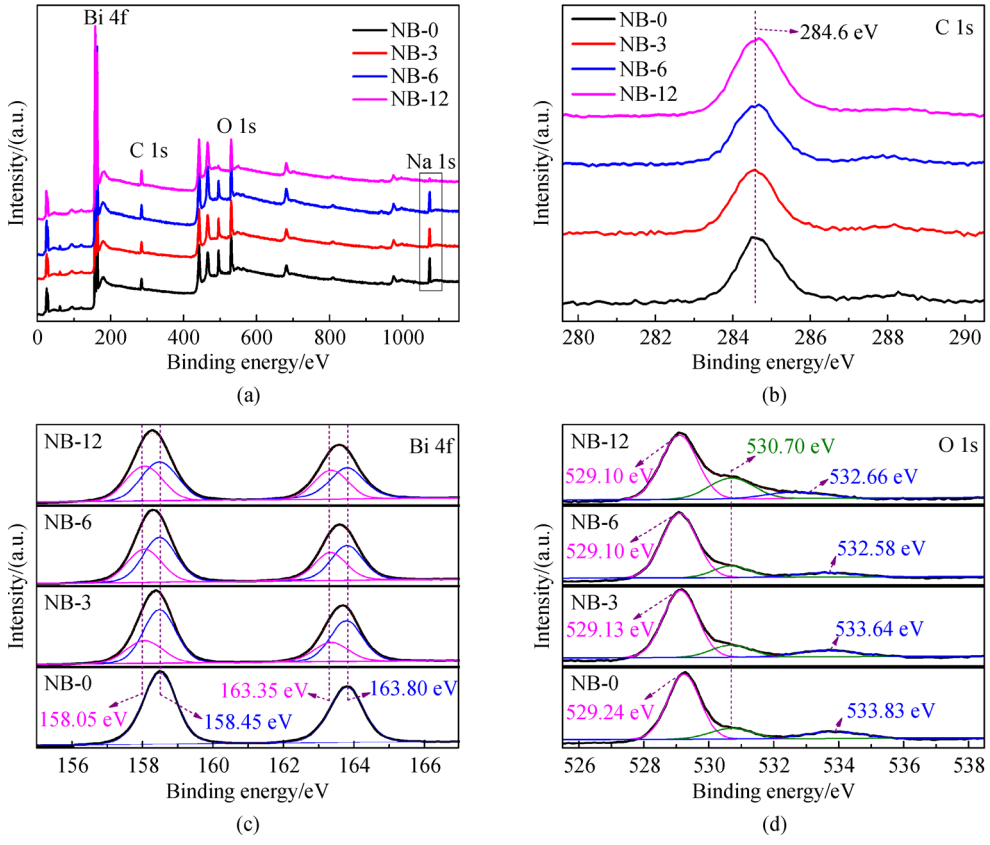


**Fig. 5** XPS spectra of NB-0, NB-3, NB-6 and NB-12.
(a) Survey scan; (b) high-resolution C 1s; (c) Bi 4f; (d) O 1s.

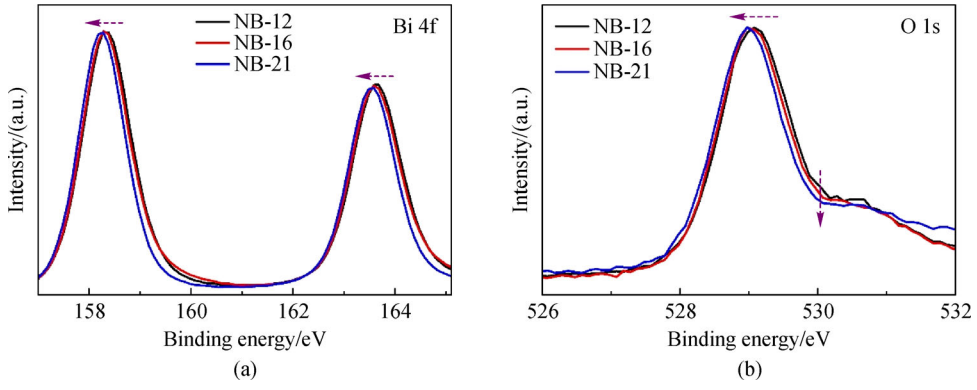


**Fig. 6** High-resolution XPS spectra of NB-12, NB-16, and NB-21.
(a) Bi 4f; (b) O 1s.

increases with the reaction time, which should be attributed to the increase of the percentage of $BiO_{2-x}$ in the composite. Accordingly, $BiO_{2-x}$ (NB-12, NB16, and NB-21) shows a much higher visible light absorption than other samples. On the other hand, detailed inspection reveals that NB-12 has the highest visible light absorption efficiency (upper panel in Fig. 7(b)), which should be attributed to the highest oxygen vacancy density in this sample. It has been reported that the oxygen vacancy could produce a defect energy level to enhance the light adsorption [43–46].

In the longer wavelength range between 900 and 1200 nm, the light absorption shows a quite different dependence on the composition (lower panel in Fig. 7(b)). It is seen that NBH has a better absorption than $BiO_{2-x}$, and accordingly, the longer wavelength light absorption decreases continuously as the amount of $BiO_{2-x}$ increases

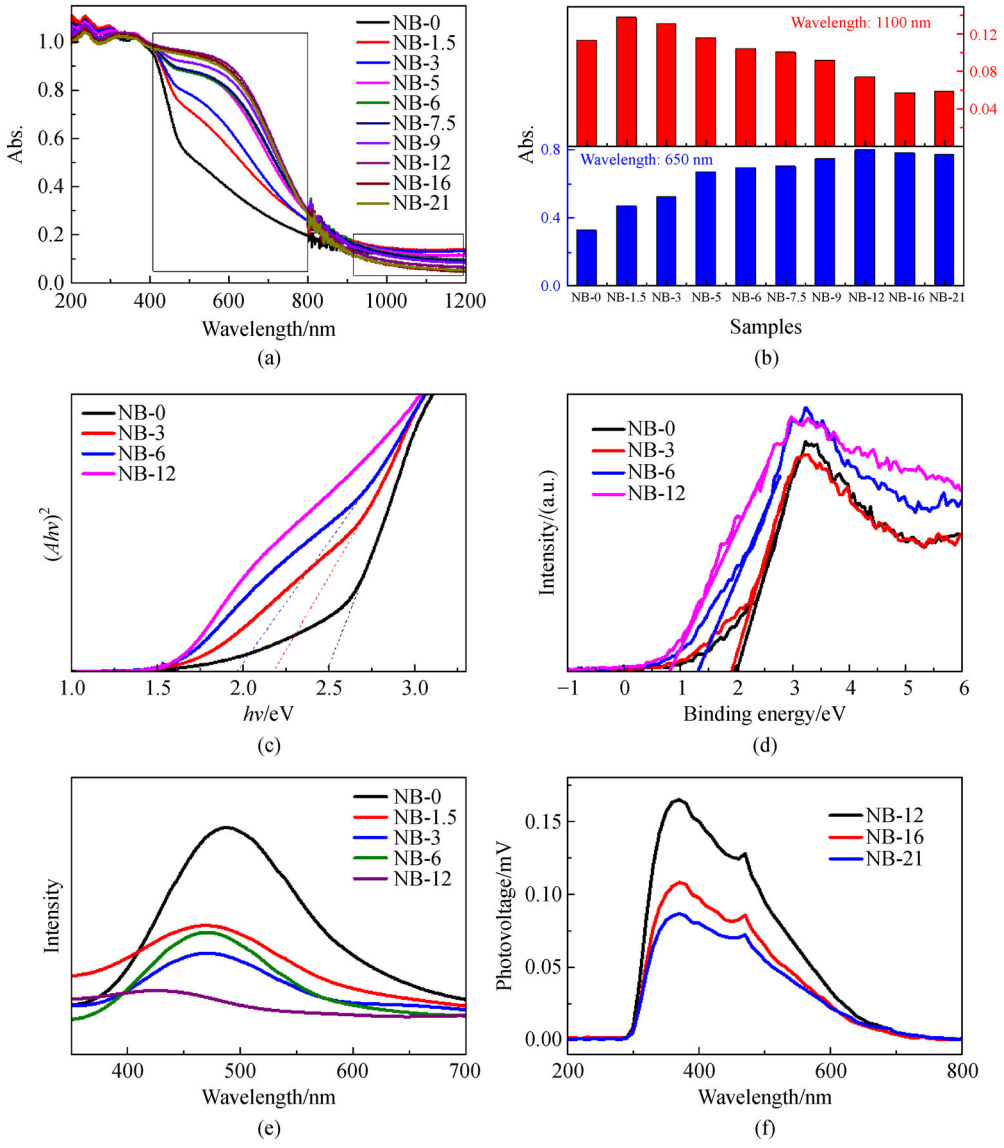


**Fig. 7** Optical properties of a series of reaction time dependent samples.
(a) UV-vis diffuse reflectance spectra; (b) Light absorption value at 650 nm and 1100 nm; (c) Tauc plots of $(Ahv)^2$ versus energy ($hv$) for the bandgap energy; (d) XPS valance plots; (e) PL spectra; (f) SPV spectra.

from the NB-1.5 sample. Interestingly, the obvious enhancement of the light absorption in NB-1.5 or NB-3 as compared with NB-0 could be probably due to the rich oxygen vacancies in the tiny $BiO_{2-x}$ plates. The concentration of oxygen vacancy will continue to decrease because of reaction time, which is consistent with the results of EDS and XPS elements analysis.

The bandgap energies of NB-0 and NB-12 estimated from the Tauc plots [47] are 2.48 and 1.60 eV, respectively, as shown in Fig. 7(c). The valance band positions measured by VB-XPS are 1.86 and 0.82 eV for NB-0 and NB-12 (Fig. 7(d)), respectively. The room-temperature PL spectra were measured to evaluate the separation efficiency of the photo-generated electron-hole pairs. In general, a decrease in the PL intensity indicates a suppressed electron-hole pair recombination [48]. As shown in Fig. 7(e), among NB-0, NB-1.5, NB-3, NB-6, and NB-12, NB-0 and NB-12 show the highest and lowest PL peak intensity, respectively. This result indicates that $BiO_{2-x}$ has a much better charge separation property than the starting material NBH. Consistently, NB-1.5, NB-6, and NB-3 show a gradually reduced PL peak intensity (NB-1.5 > NB-6 > NB-3) as compared with NB-0. The small vibration in the PL intensity should rise from the change in the composition ratio and the surface coverage of the composite. Besides, NB-16 and NB-21(not shown here) have no obvious difference with NB-12. Hence, the local electric field intensity of NB-12 to NB-21 is characterized by the steady-state surface photovoltage spectroscopy in Fig. 7(f). The highest SPV signal in NB-12

indicates the best charge separation efficiency [49], which can be attributed to the richer oxygen vacancy content in this sample. As a result, the photocurrent densities of NB-3 and NB-12 appear 2-fold higher than that of NB-0 and NB-16 (21), respectively, as shown in Fig. S2 (in ESM).

The performance of all samples was evaluated through the photocatalytic degradation of anionic dye MO. Figure 8(a) suggests that NB-0 has the lowest photocatalytic performance, with only 40% MO degraded within 120 min. On the other hand, NBH/$BiO_{2-x}$ composites possess obviously improved degradation efficiency, with NB-3 showing the best photocatalytic ability. This observation is consistent with the PL characterization results shown in Fig. 7(e), indicating that the effective separation of charge carriers dominates the photocatalytic efficiency. In addition, the enhanced light absorption ability induced by $BiO_{2-x}$ in the composite can also promote the generation of more carriers. Of the three $BiO_{2-x}$ samples, i.e., NB-12, 16, and 21, NB-12 has the highest degradation rate, even higher than all other NBH/$BiO_{2-x}$ composites (Fig. 8(b)). The superior photocatalytic ability in $BiO_{2-x}$ can be probably attributed to the better light absorption with the higher photocurrent density and richer content of oxygen vacancy with a better adsorption ability. Figure S3 shows the adsorption capacities of NB-0, NB-3, NB-12, NB-16, and NB-21 to methyl orange in the equilibrium step under dark. $BiO_{2-x}$ presents a stronger adsorption ability than NBH, which may be caused by the charge environment on the surface or a larger specific surface area. $BiO_{2-x}$ with richer oxygen defects shows a slightly higher adsorption ability than the other two. The degradation efficiencies were analyzed in more detail using quasi-first-order kinetic calculation with

$$\ln(C_0/C_t) = kt,$$

where $k$ is the quasi-first-order rate constant, $C_0$ is the equilibrium concentration of MO, and $C_t$ is the concentration at time $t$. Interestingly, NB-3 and NB-12 show the two dominant peaks in the degradation rate as plotted in Fig. 8(d), consistent with the investigations from PL, SPV, and photocurrent characterizations.

The above observations suggest that the light absorption ability, morphology, gradient composition, and the concentration of oxygen vacancies should affect the production of electrons and holes, exposed active sites, the charge separation at the hetero-interface, and intrinsic properties, which in turn determine the photocatalytic performance. In the NBH/$BiO_{2-x}$ composite, the proper band positions of NBH and $BiO_{2-x}$ support the transfer of electrons from $BiO_{2-x}$ to NBH, and the induced holes from NBH to

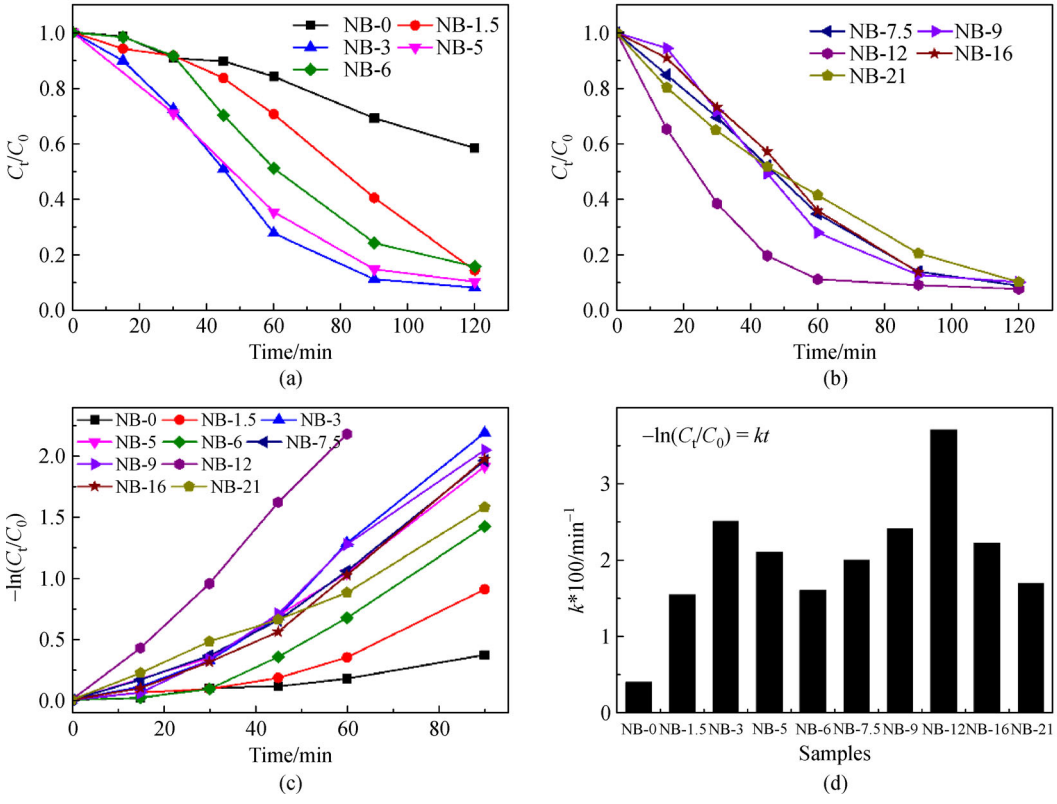


**Fig. 8** Degradation of MO using various samples under light irradiation.

(a) Evolution of concentration of NB-0, NB-1.5, NB-3, NB-5, NB-6; (b) evolution of concentration of NB-7.5, NB-9, NB-12, NB-16, NB-21; (c) kinetic fit curves of NB-0, NB-1.5, NB-3, NB-5, NB-6, NB-7.5, NB-9, NB-12, NB-16, NB-21; (d) degradation rate value $k$ for NB-0, NB-1.5, NB-3, NB-5, NB-6, NB-7.5, NB-9, NB-12, NB-16, NB-21.

$BiO_{2-x}$ (Fig. 9(a)). The NBH conduction band has a more negative reduction potential than $O_2$/couple, which can support the generation of $O_2^{-\bullet}$ or be further converted into ·OH. In addition to the photogenerated holes on the valence band of $BiO_{2-x}$, the reactive oxygen radicals could also support the degradation of methyl orange. As shown in Fig. 10(a), the scavenger test results of NB-3 prove the existence and function of reactive oxygen radicals and holes, in the measurements, the $O_2^{-\bullet}$, •OH and $h^+$ species were captured by using Benzoquinone, isopropyl alcohol and EDTA-2Na, respectively. Among all NBH/$BiO_{2-x}$ composites, NB-3 seemed to possess the optimized morphology and gradient composition, which leads to more available reaction sites and a more efficient charge separation. However, in the case of NB-6, as shown in the SEM image, the NBH sheets are mostly covered by $BiO_{2-x}$, hence, the reactive sites on the component of NBH could not expose to the reactive species, resulting in a bad photocatalytic performance. After NB-6, both NBH and $BiO_{2-x}$ are exposed, resulting in the recovery of the photocatalytic performance. In $BiO_{2-x}$ samples, the surface oxygen vacancies in $BiO_{2-x}$ could act as catalytic centers as shown in Fig. 9(b). The photogenerated electrons can be captured in oxygen vacancy, and participate in the rapid activation of $O_2$ to $O_2^{-\bullet}$ [50,51]. Furthermore, the oxygen vacancy could promote more adsorption of anionic molecular on the surface of $BiO_{2-x}$, which also helps in improving the degradation of MO. The scavenger test results of NB-12 in Fig. 10(b) also proves the existence and function of reactive oxygen radicals and holes. However, in the test of holes, the EDTA-2Na may also be adsorbed on the surface of the catalyst and block the active sites, resulting in a huge drop in degradation performance. Both NB-3 and NB-12 show a good stability as shown in Fig. S4 (in ESM). The recycle experiments show that the degradation efficiencies remain relatively stable. There is no obvious change between the XRD patterns of fresh and used samples. Based on the obtained investigations, the degradation efficiency and photocurrent decreases with the decrease of the concentration of oxygen vacancy in $BiO_{2-x}$. It can be inferred that $BiO_{2-x}$ formed with different reaction times should present different photocatalytic

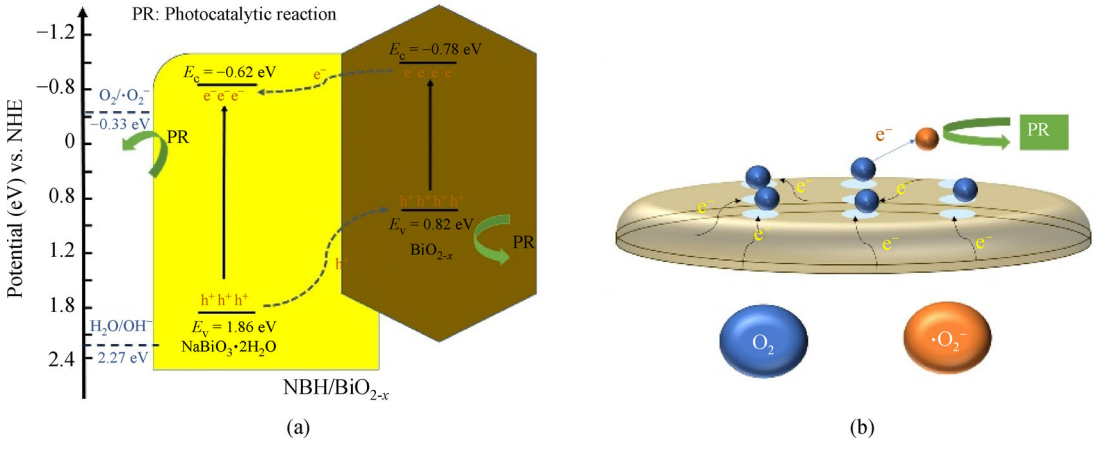


**Fig. 9** Mechanism of photocatalytic degradation process.
(a) Purposed charge transfer of NBH/$BiO_{2-x}$ composite; (b) schematic illustration of rich oxygen vacancy on the surface of $BiO_{2-x}$.

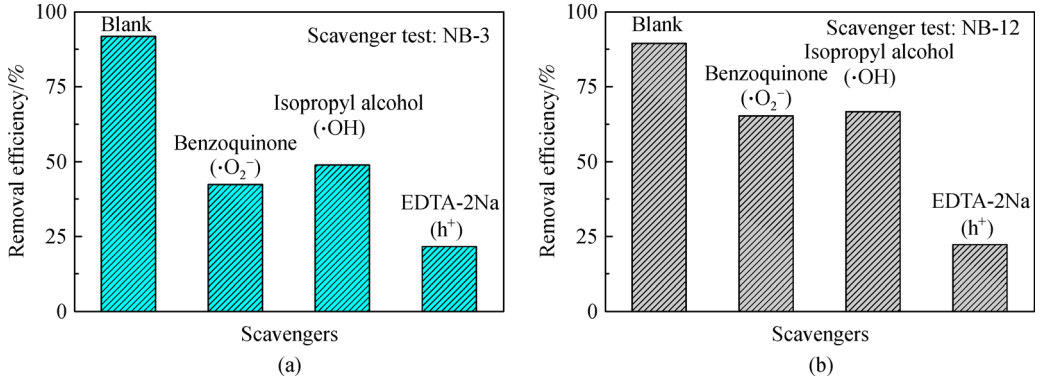


**Fig. 10** Scavenger tests of samples.
(a) NB-3; (b) NB-12.

properties, due to the evolution of the oxygen vacancy. Consequently, to construct a composite system, not only the fraction and distribution of each component, but also the property evolution of each component during the coupling process should be considered. Based on the SEM, XRD, and XPS characterization results, the phase transition process based on the structure and reaction time is manifested in Scheme 1.

Furthermore, to investigate the photocatalytic reduction abilities of the NB-3 composite and $BiO_{2-x}$, the measurements of photocatalytic $CO_2$ reduction in a solid/gas system were conducted. The main product of all the measurements is CO gas, as shown in Fig. 11, where very small amount of $CH_4$ can be observed. The performance of sample NB-3 is higher than that of NBH regarding the CO production rate, which is consistent with the trend observed in the degradation test. It could be attributed to the stronger light absorption ability and efficient separation of electrons and holes in NB-3. Interestingly, the $BiO_{2-x}$ (NB-12) shows a poor performance in the photoreduction of $CO_2$. This should be attributed to the surface of $BiO_{2-x}$ which is not conducive to the reduction of $CO_2$. Therefore, for a photocatalyst, the surface activity to different reactants also directly affects the catalytic performance. The investigation of surface activity will be performed in future work.

## 4 Conclusions

An *in situ* phase transition process under hydrothermal reaction is proposed. This process is helpful to analyze the factors that affect the catalytic performance in a composite. In the gradient phase transition process from NBH to $BiO_{2-x}$, determined by the reaction time, the fraction and distribution between NBH and $BiO_{2-x}$ in the NBH/$BiO_{2-x}$ composite directly affect the morphology. A proper amount of $BiO_{2-x}$ on the surface of NBH could effectively suppress the electron/hole recombination and increase the exposed reactive sites for photocatalytic reaction. A fully

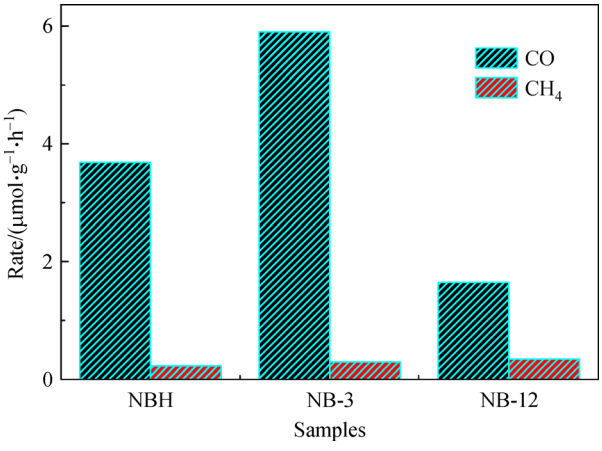


**Fig. 11** Photocatalytic conversion rates of $CO_2$ to CO and $CH_4$ based on the samples of NBH, NB-3, and NB-12.

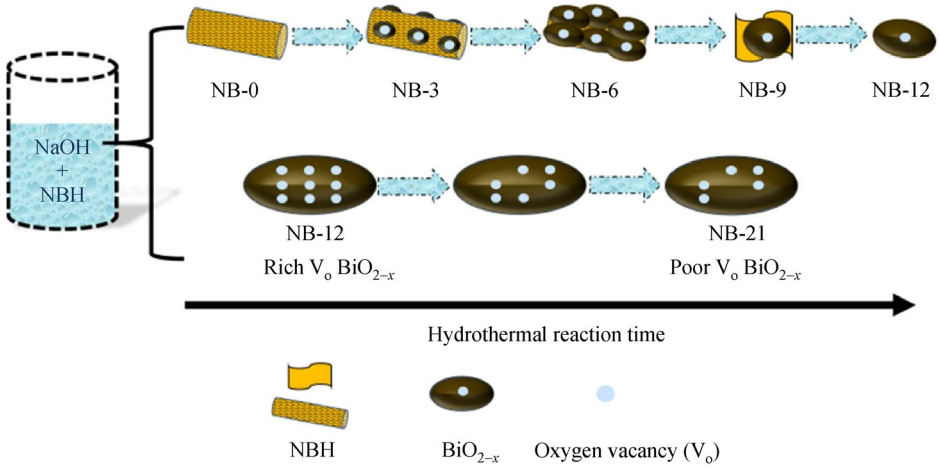


**Scheme 1** Phase transition process based on the structure and reaction time.

covered $BiO_{2-x}$ on $NaBiO_3 \cdot 2H_2O$ results in a dramatical decrease of photocatalytic performance, due to the inhibited reactive sites. An over long hydrothermal process can result in $BiO_{2-x}$ with a reduced oxygen vacancy, which degrades the photocatalytic activity. This phenomenon reveals that the defects in $BiO_{2-x}$ could be affected by the process of constructing a $BiO_{2-x}$ based composite. This study presents clear information of the factors that can affect the photocatalytic performance. It also illustrates that in addition to selecting gradient materials with suitable bandgap structures, the composition and morphology, the evolution of oxygen vacancy content or defect in a component is also an important factor that should be optimized to achieve high photocatalytic efficiency.

**Acknowledgements** This research was supported by the Basic Science Research Program through the National Research Foundation of Korea funded by the Ministry of Science, ICT and Future Planning (2017R1D1A1B03032265 and 2019R1A2C1086881). SEM characterization in this research was supported by Nano-material Technology Development Program through the National Research Foundation of Korea (NRF) funded by the Ministry of Science, ICT and Future Planning (2009-0082580).

**Electronic Supplementary Material** Supplementary material is available in the online version of this article at https://doi.org/10.1007/s11708-021-0778-4 and is accessible for authorized users.

## References

1. Kudo A, Miseki Y. Heterogeneous photocatalyst materials for water splitting. Chemical Society Reviews, 2009, 38(1): 253–278
2. Dong X, Li J, Xing Q, et al. The activation of reactants and intermediates promotes the selective photocatalytic NO conversion on electron-localized Sr-intercalated g-$C_3N_4$. Applied Catalysis B: Environmental, 2018, 232: 69–76
3. Jia Y, Wu C, Lee B W, et al. Magnetically separable sulfur-doped $SnFe_2O_4$/graphene nanohybrids for effective photocatalytic purification of wastewater under visible light. Journal of Hazardous Materials, 2017, 338: 447–457
4. Wang M, Artero V, Hammarström L, et al. Molecular catalysts for artificial photosynthesis: general discussion. Faraday Discussions, 2017, 198: 353–395
5. Chen L, Zhang W, Wang J, et al. High piezo/photocatalytic efficiency of $Ag/Bi_5O_7I$ nanocomposite using mechanical and solar energy for $N_2$ fixation and methyl orange degradation. Green Energy and Environment, 2021, online, https://doi.org/10.1016/j.gee.2021.04.009
6. Zhang W, Xing P, Zhang J, et al. Facile preparation of novel nickel sulfide modified $KNbO_3$ heterojunction composite and its enhanced performance in photocatalytic nitrogen fixation. Journal of Colloid and Interface Science, 2021, 590: 548–560
7. Chen P, Chen L, Ge S, et al. Microwave heating preparation of phosphorus doped g-$C_3N_4$ and its enhanced performance for photocatalytic $H_2$ evolution in the help of $Ag_3PO_4$ nanoparticles. International Journal of Hydrogen Energy, 2020, 45(28): 14354–14367
8. Zhuge Z, Liu X, Chen T, et al. Highly efficient photocatalytic degradation of different hazardous contaminants by $CaIn_2S_4$-$Ti_3C_2T_x$ Schottky heterojunction: an experimental and mechanism study. Chemical Engineering Journal, 2021, 421: 127838
9. Zhang X, Tian F, Qiu L, et al. Z-Scheme $Mo_2C/MoS_2/In_2S_3$ dual-heterojunctions for the photocatalytic reduction of Cr(VI). Journal of Materials Chemistry A, Materials for Energy and Sustainability, 2021, 9(16): 10297–10303
10. Bao S, Wang Y, Wei Z, et al. Amino-assisted AHMT anchored on graphene oxide as high performance adsorbent for efficient removal of Cr(VI) and Hg(II) from aqueous solutions under wide pH range. Journal of Hazardous Materials, 2021, 416: 125825
11. Bao S, Yang W, Wang Y, et al. Highly efficient and ultrafast removal of Cr(VI) in aqueous solution to ppb level by poly(allylamine hydrochloride) covalently cross-linked amino-modified graphene oxide. Journal of Hazardous Materials, 2021, 409: 124470
12. Ma H, Jia Y, Zhu G, et al. Study of cyano and hydroxyl groups modification on the properties of porous carbon nitride synthesized by using a salt assistant method. Applied Surface Science, 2020, 507: 144885
13. Cao S, Low J, Yu J, et al. Polymeric photocatalysts based on graphitic carbon nitride. Advanced Materials, 2015, 27(13): 2150–2176
14. Meng X, Zhang Z. Bismuth-based photocatalytic semiconductors: introduction, challenges and possible approaches. Journal of Molecular Catalysis A Chemical, 2016, 423: 533–549
15. McFarland E W, Metiu H. Catalysis by doped oxides. Chemical Reviews, 2013, 113(6): 4391–4427
16. Wang H, Zhang L, Chen Z, et al. Semiconductor heterojunction photocatalysts: design, construction, and photocatalytic performances. Chemical Society Reviews, 2014, 43(15): 5234
17. Liu X, Liu B, Li L, et al. $Cu_2In_2ZnS_5/Gd_2O_2S$: Tb for full solar spectrum photoreduction of Cr(VI) and $CO_2$ from UV/vis to near-infrared light. Applied Catalysis B: Environmental, 2019, 249: 82–90
18. Liu X, Liu H, Wang Y, et al. Nitrogen-rich g-$C_3N_4$@AgPd Mott-Schottky heterojunction boosts photocatalytic hydrogen production from water and tandem reduction of and. Journal of Colloid and Interface Science, 2021, 581: 619–626
19. Wang Y, Bao S, Liu Y, et al. Efficient photocatalytic reduction of Cr (VI) in aqueous solution over $CoS_2$/g-$C_3N_4$-rGO nanocomposites under visible light. Applied Surface Science, 2020, 510: 145495
20. Feng Z, Zeng L, Zhang Q, et al. *In situ* preparation of g-$C_3N_4$/$Bi_4O_5I_2$ complex and its elevated photoactivity in methyl orange degradation under visible light. Journal of Environmental Sciences (China), 2020, 87: 149–162
21. Wei Z, Zhu Y, Guo W, et al. Enhanced photocatalytic overall water splitting via MOF-derived tetragonal $BiVO_4$-based solid solution. Chemical Engineering Journal, 2021, 414: 128911
22. Wei Z, Zhu Y, Guo W, et al. Enhanced twisting degree assisted overall water splitting on a novel nano-dodecahedron $BiVO_4$-based heterojunction. Applied Catalysis B: Environmental, 2020, 266: 118664
23. Usai S, Obregón S, Becerro A I, et al. Monoclinic-tetragonal heterostructured $BiVO_4$ by yttrium doping with improved photocatalytic activity. Journal of Physical Chemistry C, 2013, 117(46):

24479–24484

24. Li H, Hu D, Li Z, et al. Emerging layered $BiO_{2-x}$ for photocatalysis: status, challenges, and outlook. Sustainable Energy & Fuels, 2020, 4 (11): 5378–5386
25. Li J, Wu X, Pan W, et al. Vacancy-rich monolayer $BiO_{2-x}$ as a highly efficient UV, visible, and near-infrared responsive photocatalyst. Angewandte Chemie, 2018, 130(2): 500–504
26. Mao Y, Wang P, Li L, et al. Unravelling the synergy between oxygen vacancies and oxygen substitution in $BiO_{2-x}$ for efficient molecular-oxygen activation. Angewandte Chemie International Edition, 2020, 59(9): 3685–3690
27. Kumada N, Kinomura N, Sleight A W. Ion-exchange reaction of $Na^+$ in $NaBiO_3 \cdot nH_2O$ with $Sr^{2+}$ and $Ba^{2+}$. Solid State Ionics, 1999, 122(1–4): 183–189
28. Rao P S, Hayon E. Experimental determination of the redox potential of the superoxide radical. Biochemical and Biophysical Research Communications, 1973, 51(2): 468–473
29. Jia Y, Li S, Gao J, et al. Highly efficient $(BiO)_2CO_3$-$BiO_{2-x}$-graphene photocatalysts: Z-Scheme photocatalytic mechanism for their enhanced photocatalytic removal of NO. Applied Catalysis B: Environmental, 2019, 240: 241–252
30. Wang M, Tan G, Zhang D, et al. Defect-mediated Z-scheme $BiO_{2-x}$ / $Bi_2O_{2.75}$ photocatalyst for full spectrum solar-driven organic dyes degradation. Applied Catalysis B: Environmental, 2019, 254: 98–112
31. Jia Y, Li S, Ma H, et al. Oxygen vacancy rich $Bi_2O_4$-$Bi_4O_7$-$BiO_{2-x}$ composites for UV-vis-NIR activated high efficient photocatalytic degradation of bisphenol A. Journal of Hazardous Materials, 2020, 382: 121121
32. Li J, Li Y, Zhang G, et al. One-dimensional/two-dimensional core–shell-structured $Bi_2O_4$/$BiO_{2-x}$ heterojunction for highly efficient broad spectrum light-driven photocatalysis: faster interfacial charge transfer and enhanced molecular oxygen activation mechanism. ACS Applied Materials & Interfaces, 2019, 11(7): 7112–7122
33. Wang J, Liu Z, Liu Z. $BiO_{2-x}$/$NaBiO_3$ hybrid composites: facile synthesis, enhanced photocatalytic activity and mechanism. Solid State Sciences, 2019, 95: 105935
34. Dias A, Moreira R L. Crystal structure and phonon modes of ilmenite-type $NaBiO_3$ investigated by Raman and infrared spectroscopies. Journal of Raman Spectroscopy: JRS, 2010, 41(6): 698–701
35. Li L, Liu Z, Guo L, et al. $NaBiO_3$/$BiO_{2-x}$ composite photocatalysts with post-illumination "memory" activity. Materials Letters, 2019, 234: 30–34
36. Lu Y, Huang Y, Zhang Y, et al. Oxygen vacancy engineering of $Bi_2O_3$/$Bi_2O_2CO_3$ heterojunctions: implications of the interfacial charge transfer, NO adsorption and removal. Applied Catalysis B: Environmental, 2018, 231: 357–367
37. Mao Y, Wang P, Li L, et al. Unravelling the synergy between oxygen vacancies and oxygen substitution in $BiO_{2-x}$ for efficient molecular-oxygen activation. Angewandte Chemie International Edition, 2020, 59(9): 3685–3690
38. Li L, Chen T, Liu Z, et al. Novel $BiO_{2-x}$ photocatalyst: typical hierarchical architecture and commendable activity. Materials Letters, 2018, 212: 267–270
39. Jia Y, Ma H, Liu C. Au nanoparticles enhanced Z-scheme Au-$CoFe_2O_4$/$MoS_2$ visible light photocatalyst with magnetic retrievability. Applied Surface Science, 2019, 463: 854–862
40. Ding Y, Yang F, Zhu L, et al. $Bi^{3+}$ self-doped $NaBiO_3$ nanosheets: facile controlled synthesis and enhanced visible light photocatalytic activity. Applied Catalysis B: Environmental, 2015, 164: 151–158
41. Wu J, Chen Y, Pan L, et al. Multi-layer monoclinic $BiVO_4$ with oxygen vacancies and $V^{4+}$ species for highly efficient visible-light photoelectrochemical applications. Applied Catalysis B: Environmental, 2018, 221: 187–195
42. Rossell M D, Agrawal P, Borgschulte A, et al. Direct evidence of surface reduction in monoclinic $BiVO_4$. Chemistry of Materials, 2015, 27(10): 3593–3600
43. Li X, Zhang W, Li J, et al. Transformation pathway and toxic intermediates inhibition of photocatalytic NO removal on designed Bi metal@defective $Bi_2O_2SiO_3$. Applied Catalysis B: Environmental, 2019, 241: 187–195
44. Wang J, Wang Z, Huang B, et al. Oxygen vacancy induced band-gap narrowing and enhanced visible light photocatalytic activity of ZnO. ACS Applied Materials & Interfaces, 2012, 4(8): 4024–4030
45. Liu Q, Wang F, Lin H, et al. Surface oxygen vacancy and defect engineering of $WO_3$ for improved visible light photocatalytic performance. Catalysis Science & Technology, 2018, 8(17): 4399–4406
46. Sachs M, Park J S, Pastor E, et al. Effect of oxygen deficiency on the excited state kinetics of $WO_3$ and implications for photocatalysis. Chemical Science (Cambridge), 2019, 10(22): 5667–5677
47. Tauc J, Grigorovici R, Vancu A. Optical properties and electronic structure of amorphous germanium. Physica Status Solidi. B, Basic Research, 1966, 15(2): 627–637
48. Niu M, Cheng D, Cao D. Understanding the mechanism of photocatalysis enhancements in the graphene-like semiconductor sheet/$TiO_2$ composites. Journal of Physical Chemistry C, 2014, 118 (11): 5954–5960
49. Fan H, Wang D, Xie T, et al. The preparation of high photocatalytic activity nano-spindly Ag-$BiVO_4$ and photoinduced carriers transfer properties. Chemical Physics Letters, 2015, 640: 188–193
50. Pei D, Gong L, Zhang A, et al. Defective titanium dioxide single crystals exposed by high-energy {001} facets for efficient oxygen reduction. Nature Communications, 2015, 6(1): 8696
51. Pan X, Yang M, Fu X, et al. Defective $TiO_2$ with oxygen vacancies: synthesis, properties and photocatalytic applications. Nanoscale, 2013, 5(9): 3601–3614